INTERNATIONAL JOURNAL FOR NUMERICAL METHODS IN FLUIDS
Int. J. Numer. Meth. Fluids 2003; **42**:1249–1261 (DOI: 10.1002/fld.594)

Discontinuous Galerkin spectral element lattice Boltzmann method on triangular element

Xing Shi[1], Jianzhong Lin[1,*,†] and Zhaosheng Yu[2]

[1] *Department of Mechanics, the State Key Laboratory of Fluid Power Transmission and Control, Zhejiang University, Hangzhou 310027, People's Republic of China*
[2] *Department of Mechanical and Mechatronic Engineering, University of Sydney, NSW 2006, Australia*

SUMMARY

Discontinuous Galerkin spectral element method is used to solve the lattice Boltzmann equation (LBE) in the discrete velocity space. The triangular elements are adopted because of their flexibility to deal with complex geometries. The flow past a circular cylinder is simulated by the proposed scheme. The results are consistent with those obtained from the previous numerical methods and experiments. Copyright © 2003 John Wiley & Sons, Ltd.

KEY WORDS: lattice Boltzmann; spectral element; discontinuous Galerkin method

1. INTRODUCTION

In recent years, the lattice Boltzmann method (LBM), as an alternative approach to solve the fluid flows, has aroused much attention of physics and engineering researchers. It has been applied in various areas such as hydrodynamics, multiphase flows and magnetohydrodynamics. The applications of LBM are reviewed in Reference [1].

However, there are still several limitations in the use of LBM. One of them is that the classic LBM is used only in collaboration with the uniform rectangular meshes and consequently the complex boundaries cannot be coped with. There are mainly three remedies. The first is to transform an irregular domain into a regular one by the interpolation and mapping technology. He *et al.* [2] extended LBM to the non-uniform rectangular meshes. The grid information of the density distribution function is interpolated from the square lattice. In the investigation of the flow past a circular cylinder [3], they mapped the circular region into a rectangular one. The no-slip wall boundary condition was exactly enforced on the cylinder boundary, resulting in a higher computational accuracy compared with the previous LBM simulations.

---

[*] Correspondence to: Lin Jianzhong, Department of Mechanics, the State Key Laboratory of Fluid Power Transmission and Control, Zhejiang University, Hangzhou 310027, People's Republic of China.
[†] E-mail: mecjzlin@public.zju.edu.cn

Contract/grant sponsor: National Natural Science Foundation of China; contract/grant number: 19925210

Received 20 April 2002
Revised 16 October 2002

Copyright © 2003 John Wiley & Sons, Ltd.

The second is the finite volume lattice Boltzmann method (FVLBM), which was first proposed by Nannelli and Succi [4] and then extended to the three-dimensional (3D) case by Xi *et al.* [5]. This scheme allows for implementation of LBM on the unstructured meshes with arbitrary connectivity. The function in each element has the bilinear or trilinear form, which reduces the computational accuracy to some degree. FVLBM has been successfully used in the study of the flow past a bluff body, 3D channel flow, the shear flow and so on.

The third is the adaptive LBGK method [6], which is still based on the square lattice. A local second-order grid refinement scheme and a boundary fitting scheme were proposed in Reference [6]. It is helpful to improve the resolving ability of the curved boundary and the computational accuracy in the regions where large gradients of solution are expected.

Among above methods, we prefer the unstructured mesh for its flexibility to deal with complex boundary. We found that low order accurate schemes may introduce excessive artificial dissipation in the solution. Therefore, we employ the spectral element method that has the exponential convergence. The discontinuous Galerkin method [7–10] is chosen because it is very suitable for parallel computations.

2. NUMERICAL METHODS

2.1. Lattice Boltzmann method

Unlike traditional numerical schemes based on the discretization of macroscopic continuum equations, the Boltzmann equation is established from the microscopic perspective. Actually, the Navier–Stokes equation is the second-order approximation of the Boltzmann equation. Because the Boltzmann equation describes the evolution of the density distribution function, in some sense it reveals that the fluid motion is another type of particle motion. In this section, we will describe the discrete form of the Boltzmann equation with a single relaxation time. The original LBE in the discrete velocity space is given as

$$\frac{\partial f_i}{\partial t} + \mathbf{e}_i \cdot \nabla f_i = \Omega_i \tag{1}$$

where f_i is the density distribution function, $\mathbf{e}_i$ is the streaming velocity in the ith direction in the phase space, $i = 1, 2, \ldots, N$, and Ω_i represents the collation operator. In the incompressible LGBK model as described in References [11–13],

$$\Omega_i = -\frac{1}{\varepsilon\tau}(f_i - f_i^{\text{eq}})$$

f_i^{eq} is the local equilibrium distribution, τ is the single relaxation time, and ε is the small parameter which is proportional to the Knudsen number. The GBK approximation greatly simplifies the form of collation operator and makes the computation more efficient. In the simulation, f_i^{eq} is taken as

$$f_i^{\text{eq}} = \rho w_i \left(1 + \frac{3}{c^2}\mathbf{e}_i \cdot \mathbf{u} + \frac{9}{2c^4}(\mathrm{e}_i \cdot \mathbf{u})^2 - \frac{3u^2}{2c^2} \right) \quad i = 0, \ldots, n \tag{2}$$

where ρ and $\mathbf{u}$ are the macroscopic fluid density and velocity, respectively, which are calculated by

$$\rho = \sum_i f_i$$

$$\mathbf{u} = \frac{1}{\rho} \sum_i f_i \mathbf{e}_i$$

In the 9-bit LBGK model chosen in this study, the 2D velocity in the phase space is discretized in nine directions:

$$\mathbf{e}_0 = 0$$

$$\mathbf{e}_i = (\cos(\pi(i-1)/2, \sin(\pi(i-1)/2)), \quad i = 1\text{–}4$$

$$\mathbf{e}_i = \sqrt{2}(\cos(\pi(i-4.5)/2, \sin(\pi(i-4.5)/2)), \quad i = 5\text{–}8$$

The kinematic viscosity for the nine-speed model is $v = \varepsilon\tau/3$ [14]. In Equation (2), w_i equals $\frac{4}{9}$ for $i = 0, \frac{1}{9}$ for $i = 1$–4, and $\frac{1}{36}$ for $i = 5$–8.

2.2. Discontinuous Galerkin spectral element method

The discontinuous Galerkin method has many advantages. It is suitable for solving the advection equation. The evolution of information on each element depend only on the element itself and the inflow information from its upwind neighbouring elements. The discontinuous Galerkin formulation for Equation (1) can be written as

$$(\phi, \partial_t f_i)_e - (\nabla\phi, \mathbf{e}_i f_i)_e + \int_{\partial e} \phi \mathbf{n} \cdot \mathbf{e}_i f_i \, \mathrm{d}l = (\phi, \Omega_i) \tag{3}$$

where the $(\cdot, \cdot)$ denotes the projection operator and ϕ, the test function and $\mathbf{n}$ is the unit outward normal vector on the surface of the element. To introduce the upwind characteristic, the Roe flux is used to evaluate the boundary integration in Equation (3). Fortunately, because Equation (1) is a linear advection equation, the Roe flux is reduced to $\mathbf{n} \cdot \mathbf{e}_i f_i^+$, while $\mathbf{n} \cdot \mathbf{e}_i < 0$, and $\mathbf{n} \cdot \mathbf{e}_i f_i^-$ while $\mathbf{n} \cdot \mathbf{e}_i > 0$, where '+' means the density distribution function on the upwind element is used for the boundary integration and '−' means the function on the element itself is used. On each element, we get the ODE in each direction of $\mathbf{e}_i$

$$\frac{\mathrm{d}}{\mathrm{d}t} F_i = L(F_i) \tag{4}$$

where

$$F_i = \int_e \phi f_i \, \mathrm{d}s$$

$$L(F_i) = \int_e \nabla\phi \cdot \mathbf{e}_i f_i \, \mathrm{d}s - \int_{\partial e} \phi \mathbf{n} \cdot \mathbf{e}_i f_i \, \mathrm{d}l + \int_e \phi \cdot \Omega_i \, \mathrm{d}s$$

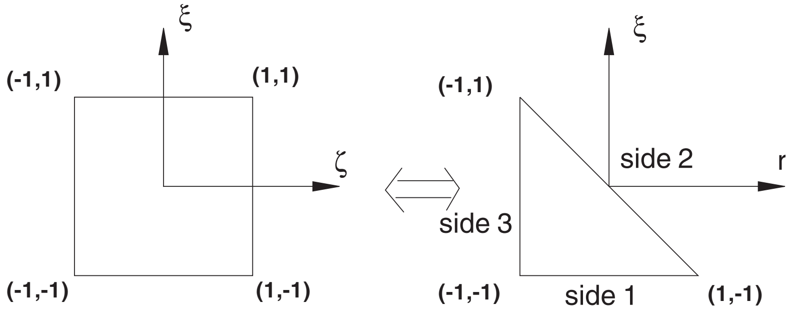

Figure 1. Schematic diagram for the mapping from the square to the standard triangle.

Dubiner's modified triangular basis [15, 16] is chosen as the test function. In fact, they can be considered to be defined on a square, and then mapped onto the standard triangle by

$$\zeta = 2\,\frac{1+r}{1-\xi} - 1$$

The mapping schematic is shown in Figure 1. Dubiner's modified triangular basis is constructed with interior and boundary modes as following:

i. Interior modes $(i>1\colon\ 1<ij<M\colon\ i+j<N)$

$$\phi_{ij} = \left(\frac{1+\zeta}{2}\right)\left(\frac{1-\zeta}{2}\right) P_{i-2}^{1,1}(\zeta) \left(\frac{1-\xi}{2}\right)^{i} \left(\frac{1+\xi}{2}\right) P_{j-1}^{2i-1,1}(\xi)$$

ii. Edge modes $(1<i;\ 0<i,j<M;\ i+j<N)$

$$\phi_{ij}^{1} = \left(\frac{1+\zeta}{2}\right)\left(\frac{1-\zeta}{2}\right) P_{i-2}^{1,1}(\zeta)\left(\frac{1-\xi}{2}\right)^{i}$$

$$\phi_{ij}^{2} = \left(\frac{1+\zeta}{2}\right)\left(\frac{1-\xi}{2}\right)\left(\frac{1+\xi}{2}\right) P_{j-1}^{1,1}(\xi)$$

$$\phi_{ij}^{3} = \left(\frac{1-\zeta}{2}\right)\left(\frac{1-\xi}{2}\right)\left(\frac{1+\xi}{2}\right) P_{j-1}^{1,1}(\xi)$$

iii. Vertex modes

$$\phi^{1} = \left(\frac{1-\zeta}{2}\right)\left(\frac{1-\xi}{2}\right)$$

$$\phi^{2} = \left(\frac{1+\zeta}{2}\right)\left(\frac{1-\xi}{2}\right)$$

$$\phi^{3} = \left(\frac{1+\xi}{2}\right)$$

where $P_n^{\alpha,\beta}(x)$ is the nth order Jacobi polynomial in the $[-1,1]$, M and N are the orders of the polynomial in two directions of the local co-ordinates respectively.

If the Gauss quadrature points are used, the integration on the element can be evaluated as

$$\int\int_e f(x,y)\,\mathrm{d}x\,\mathrm{d}y = \sum_{i=0}^{q_\zeta-1}\sum_{j=0}^{q_\xi-1} f(\zeta_i,\xi_j)J_{ij}w_i^\zeta w_j^\xi \tag{5}$$

In this paper, ζ_i and w_i^ζ denote the Gauss–Lobatto quadrature points and weights to $P^{0,0}(\zeta)$, and ξ_i, w_i^ξ are the Gauss–Radau quadrature points and weights to $P^{1,0}(\xi)$. q_ζ, q_ξ are the numbers in the ζ and ξ direction. J_{ij} is the Jacobian transform matrix from the arbitrary triangle domain to the standard triangle. However, if the sides of the triangle are straight, J_{ij} is constant on each element.

We can approximate the function f by the expansion over each triangular element:

$$f(x,y) = \sum_m\sum_n \hat{f}_{mn}\phi_{mn}(\zeta(x,y),\xi(x,y)) \tag{6}$$

where $\hat{f}_{mn}$ is expansion coefficient according to the basis function ϕ_{mn}. Based on Equations (5) and (6), Equation (4) relating to $\hat{f}_{mn}$ can be achieved. More details about triangle spectral element method can be found in Reference [16].

3. FLOW PAST A CIRCULAR CYLINDER

To demonstrate the capacity of the current scheme, we perform the simulation of the flow past a cylinder at various Reynolds numbers.

The typical unstructured mesh is shown in Figure 2. The number of elements is 1283. The lateral distance is $55D$, where D is the diameter of the cylinder. From the centre of cylinder, the inlet is $50D$ upstream and the outlet is $60D$ downstream. The order of the polynomial in both directions is 5. The flow field is initialized from an irrotational potential flow. It should be noted that the proper initial condition must be given for the method proposed in this paper, otherwise the solution would diverge. On the domain boundary the velocity is enforced with $U = 0.1$ and the density functions are evaluated with the equilibrium values. On the cylinder wall, the bounce-back rule is used to guarantee the no-slip condition. The time step must satisfy the relation (Reference [16]):

$$\Delta t \leqslant 0.723/(C(\mathbf{V},L)M^2)$$

where $C(\mathbf{V},L)$ is related to the local wave speed $\mathbf{V}$ and the characteristic length L, and M is the order of the polynomial expansion.

The drag coefficient is defined as

$$C_\mathrm{d} = \frac{1}{\rho U^2 a}\oint_l (\mathbf{S}\cdot\mathbf{n})\cdot\mathbf{n}_x\,\mathrm{d}l$$

where a is the cylinder radius, $\mathbf{S}$ is the stress tensor

$$\mathbf{S} = -p\mathbf{I} + \rho\nu(\nabla\mathbf{u} + (\nabla\mathbf{u})^\mathrm{T})$$

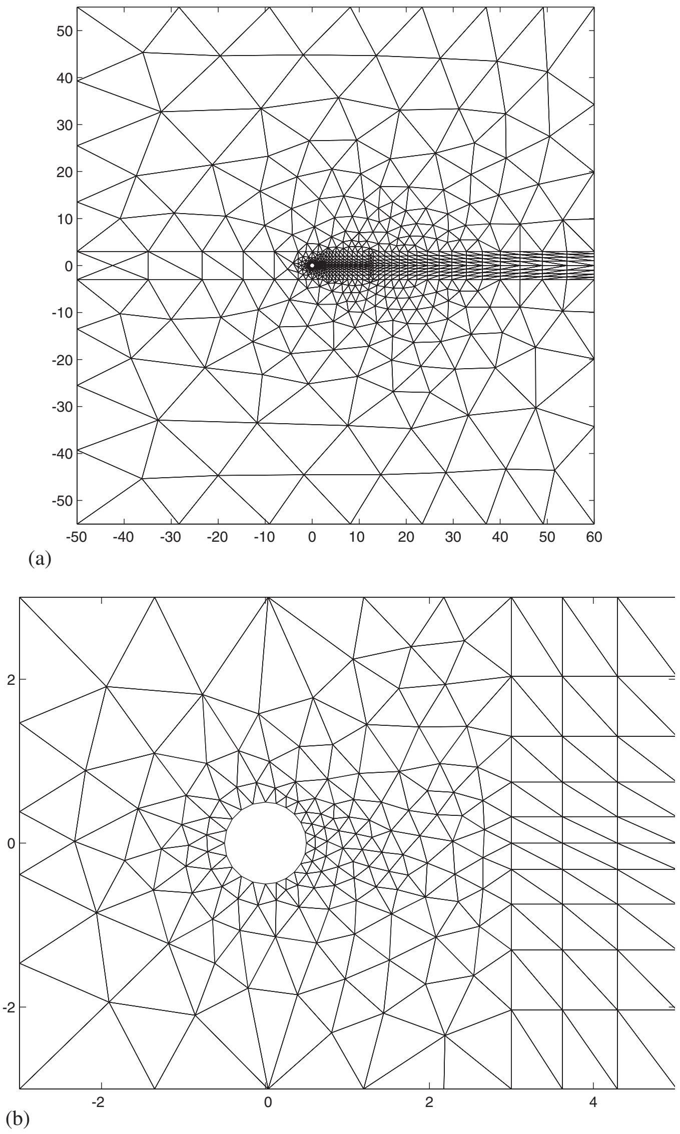

Figure 2. Meshes for the flow past a circular cylinder in (a) the entire computational domain and (b) the vicinity of the cylinder.

and $\mathbf{n}_x$ is the streamwise component of the normal $\mathbf{n}$. Note that the derivative of velocity in the stress tensor can be conveniently and accurately obtained by the matrix-multiplication operation.

Figure 3 depicts the pressure coefficient distribution on the cylinder wall. The pressure p is evaluated directly through

$$p = c_s^2 \rho$$

Copyright © 2003 John Wiley & Sons, Ltd.

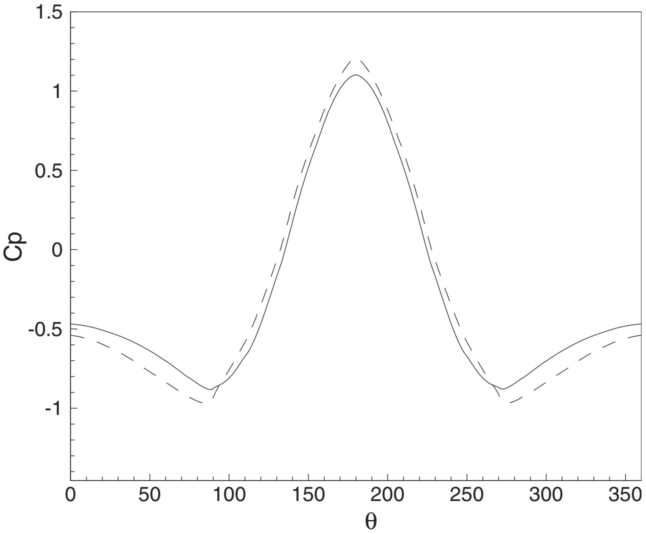

Figure 3. Pressure distribution on the cylinder wall at $Re = 20$ (solid line) and $Re = 40$ (dash line).

in 9-bit model, the sound speed $c_s = 1/\sqrt{3}$ and the pressure coefficient is defined by

$$C_p = (p - p_\infty)/0.5\rho U^2$$

From Figure 3, the distribution is not symmetrical at the front and back of the cylinder and the location of the lowest pressure is no longer the back stagnation point. As the Reynolds increases, it shifts from the back stagnation point farther and farther.

Figures 4 and 5 show the streamline and the vorticity contours at $Re = 20$ and 40 when the flow reaches the steady state. In this *Re* regime there exists a steady circulation region in the downstream of the cylinder. As the Reynolds number increases, the circulation region expands in the lateral and downstream directions. The length of the wake, the separated angle and the drag coefficient are compared with the previous results in Table I. The data given by Coutanceau and Bouard are experimental results and others are numerical ones. We can find that our computational results agree well with the previous results.

According to experimental results, when the Reynolds number is larger than 49, the flow becomes unsteady and the Karman vortex street forms with the eddies shedding alternately from the top and bottom of the cylinder at a constant frequency. The frequency of vortex shedding increases with the increasing Reynolds number. The streamline and the contours of vorticity at the time when the lift coefficient reaches the positive peak are shown in Figures 6 and 7 respectively. There are three important parameters in the periodically oscillatory flow: Strouhal number, drag coefficient and lift coefficient.

Strouhal number is used to measure the oscillating frequency nondimensionalized by the time scale D/U:

$$St = \frac{Df}{U}$$

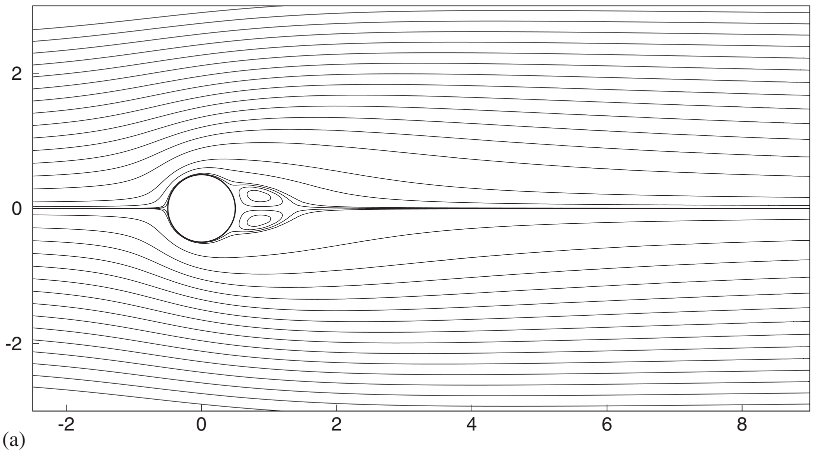

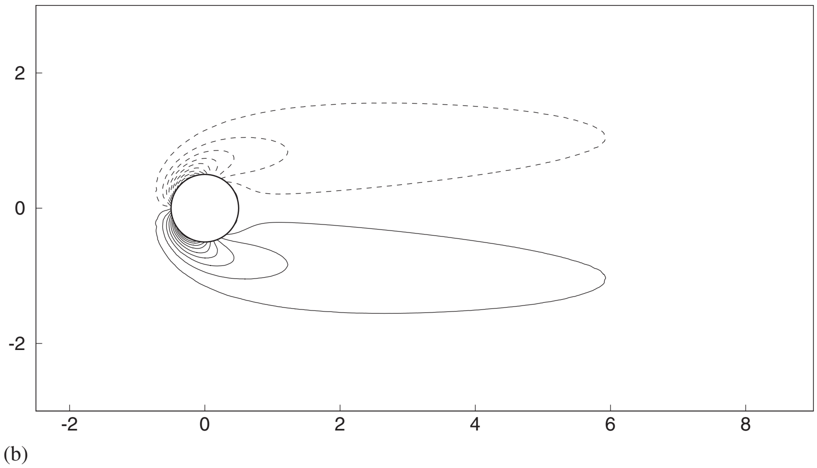

Figure 4. Steady flow past a cylinder at $Re = 20$. (a) Streamline and (b) vorticity contours. Dash and solid lines denote negative and positive levels, respectively.

where f is the frequency of vortex shedding. The lift coefficient is given as

$$C_l = \frac{1}{\rho U^2 a} \oint_l (\mathbf{S} \cdot \mathbf{n}) \cdot \mathbf{n}_y \, \mathrm{d}l$$

here, $\mathbf{n}_y$ is the y-component of $\mathbf{n}$. The integration is carried out on the cylinder wall.

The frequency of lift coefficient is half of that of drag coefficient and vortex shedding, since vortex shedding either from the top or from the bottom of the cylinder has the same effect in the streamwise direction, but has a different effect in the lateral direction. This phenomenon is reported by the previous studies [21] and is also observed in our computation.

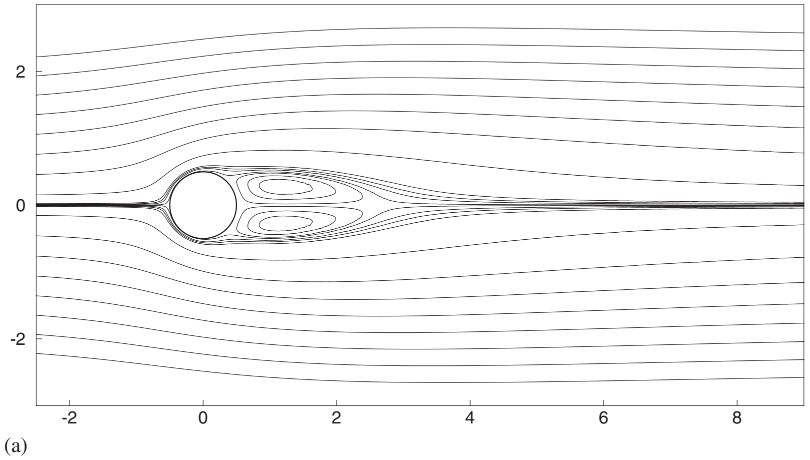

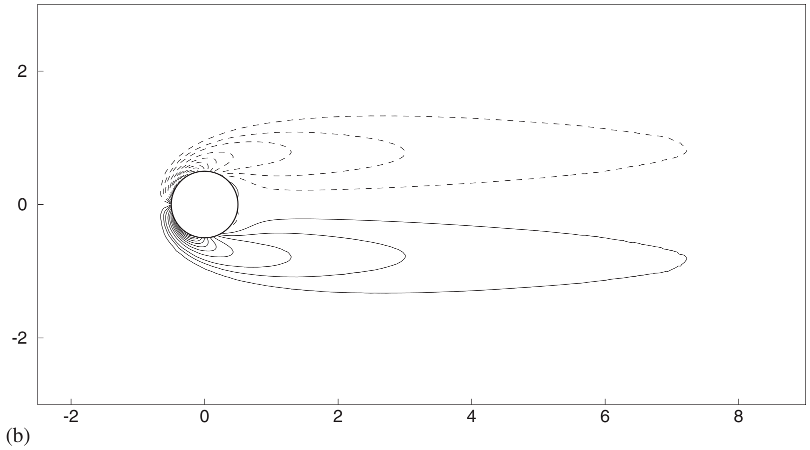

Figure 5. Steady flow past a cylinder at $Re=40$. (a) Streamline and (b) vorticity contours. Dash and solid lines denote negative and positive levels, respectively.

Table I. Comparison between present and previous results at $Re=20$ and 40.

Re	Author	L/a	θ	Cd
20	Coutanceau and Bouard [17]	1.86	44.8	
	He and Doolen [3]	1.842	42.96	2.152
	Nieuwstadt and Keller [18]	1.786	43.37	2.053
	Present	1.80	42.5	1.981
40	Coutanceau and Bouard [17]	4.26	53.5	
	He and Doolen [3]	4.49	53.34	1.550
	Nieuwstadt and Keller [18]	4.357	52.84	1.499
	Present	4.38	53.6	1.472

L: the wake length, θ: separation angle.

Copyright © 2003 John Wiley & Sons, Ltd.

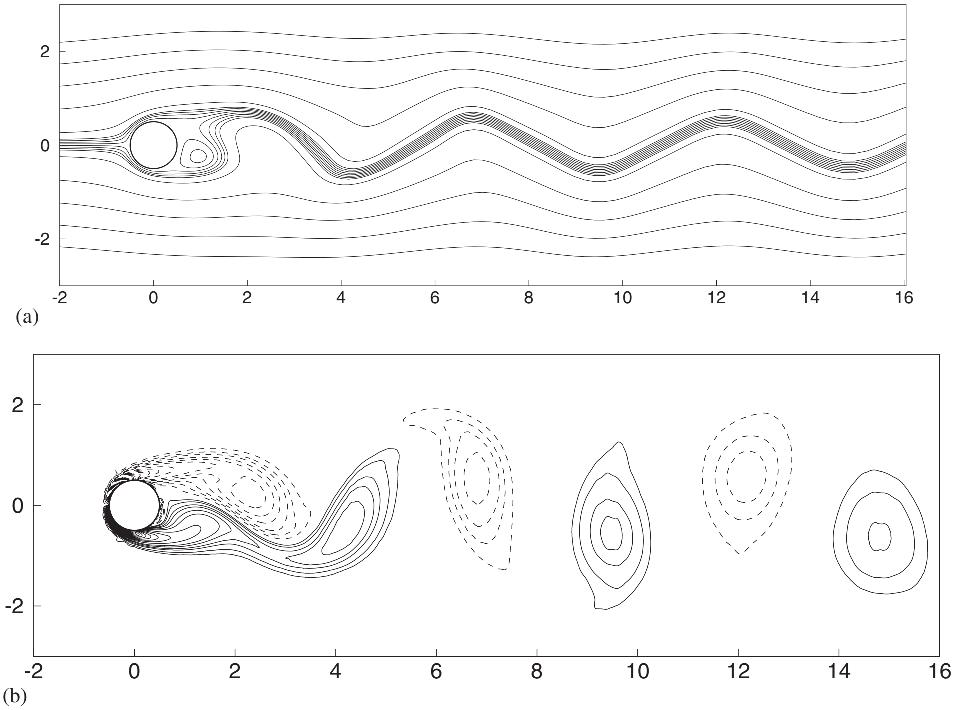

Figure 6. Unsteady flow past a cylinder at $Re = 100$. (a) Streamline and (b) vorticity contour. Dash and solid lines denote negative and positive levels, respectively.

Table II lists the Strouhal numbers, the average drag coefficients and the amplitudes of the lift coefficients as compared with the previous results. The Strouhal numbers for the results of Goldstein is evaluated by the following formula:

$$St = 0.21\left(1 - \frac{20}{Re}\right)$$

It can be found, our results are in good agreement with the others, and only the drag coefficient at $Re = 200$ seems a little higher than that of Cliffer *et al.* [19].

In Table III, the effects of the expansion order are listed. The geometry parameters and the drag coefficient are close. However, the computation with the higher-order expansion will cost more computer resource on the same mesh. The results proved that it is enough to expand to the fifth order according to the mesh used in this paper.

4. CONCLUSION

In this paper, we have extended the lattice Boltzmann method to unstructured triangular meshes for the discontinuous Galerkin spectral element method. The new scheme has been tested by

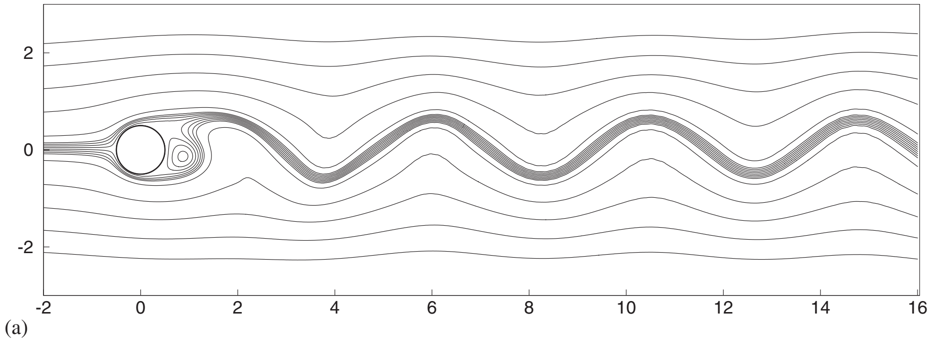

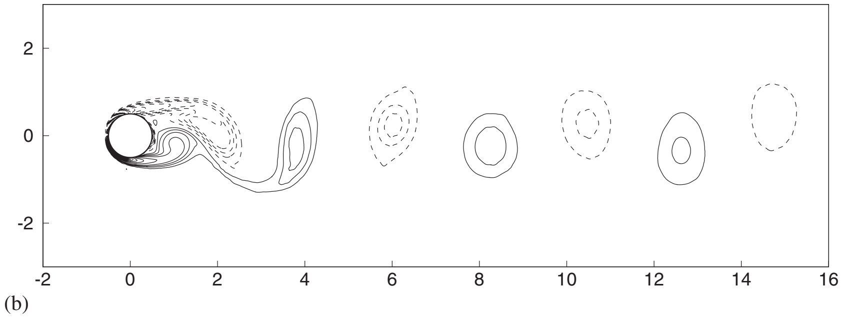

Figure 7. Unsteady flow past a cylinder at $Re = 200$. (a) Streamline and (b) vorticity contour. Dash and solid lines denote negative and positive levels, respectively.

Table II. Comparison between present and previous results at $Re = 100$ and 200.

Re	Author	St	Cd	Cl
100	Cliff *et al.* [19]		1.24	
	Braza *et al.* [21]	0.16	1.28	0.3
	Goldstein [20]	0.168		
	Present	0.161	1.29	0.32
200	Cliff *et al.* [19]		1.16	
	Braza *et al.* [21]	0.19		0.7–0.75
	Goldstein [20]	0.189		
	Present	0.191	1.27	0.7

Table III. Effects of the expansion order.

	$Re = 20$			$Re = 40$		
M	L/a	θ	Cd	L/a	θ	Cd
5	1.80	42.5	1.981	4.38	53.6	1.472
8	1.81	43.3	1.980	4.44	53.9	1.480

Copyright © 2003 John Wiley & Sons, Ltd.

the computation of the flow past a circular cylinder and the results are consistent with the previously reported ones. Our method has the following advantages:

1. *Flexibility*: It is very easy to deal with complex boundaries due to the use of unstructured triangular meshes. Compared with the classical LBM on the square meshes, unstructured meshes cause the slowdown of the computational speed. However, this can be compensated by the advantage of unstructured meshes that the adaptive technique introduces.
2. *High accuracy*: The spectral element method adopted has the exponential convergence. Although a high-order scheme leads to a higher operation count compared to low-order ones, it proves computationally more efficient if high accuracy is required.
3. *Essentially a parallel algorithm*: The spectral element method is a sort of domain decomposition method and the discontinuous Galerkin method used allows the computation to be performed on an element-by-element basis. Therefore the code is easy to make parallel.

ACKNOWLEDGEMENTS

This work was financially supported by National Natural Science Foundation of China (Grant numbers: 19925210).

REFERENCES

1. Chen S, Doolen GD. Lattice Boltzmann method for fluid flows. *Annual Reviews in Fluid Mechanics* 1998; **37**:329–364.
2. He X, Luo LS, Dembo M. Some progress in lattice Boltzmann method. Part I nonuniform mesh grids. *Journal of Computational Physics* 1996; **129**:357–363.
3. He X, Doolen GD. Lattice Boltzmann Method on curvilinear coordinates system: flow around a circular cylinder. *Journal of Computational Physics* 1997; **134**:306–315.
4. Nannelli F, Succi S. The lattice Boltzmann equation on irregular lattice. *Journal of Statistical Physics* 1992; **68**:401–407.
5. Xi H, Peng G, Chou S. Finite-volume lattice Boltzmann schemes in two and three dimensions. *Physical Review E* 1999; **60**:3380–3388.
6. Filippova O, Hanel D. Grid refinement for lattice-BGK models. *Journal of Computational Physics* 1998; **147**:219–228.
7. Reed WH, Hill TR. Technical Report LA-UR-73-479, Los Alamos Scientific Laboratory, 1973.
8. Cockburn B, Hou S, Shu CW. The Runge–Kutta local projection discontinuous Galerkin finite element method for conservation laws IV: the multidimensional case. *Mathematics of Computation* 1990; **54**:545–581.
9. Kirby RM, Wanburton TC, Lomtev I, Karniadakis GE. A discontinuous Galerkin spectral/hp method on hybrid grids. *Applied Numerical Mathematics* 2000; **33**:393–405.
10. Kershaw DS, Prasad MK, Shaw MJ, Milovich JL. 3D unstructured mesh ALE hydrodynamics with the upwind discontinuous finite element method. *Computers and Methods in Applied Mechanical Engineering* 1998; **158**:81–116.
11. Bhatnagar PL, Gross EP, Krook M. A model for collision processes in gases. 1: small amplitude processes in charged and neutral one-component system. *Physical Review* 1954; **94**:511–525.
12. Chen S, Chen H, Martinez D, Matthaeus W. Lattice Boltzmann model for simulation of magnetohydrodynamics. *Physical Review Letters* 1991; **67**:3376–3379.
13. Qian Y, d'Humieres D, Lallemand P. Lattice BGK models for Navier–Stokes equation. *Europhysics Letters* 1992; **17**:479–484.
14. Cao N, Chen S, Jin S, Martinez D. Physical symmetry and lattice symmetry in the lattice Boltzmann method. *Physical Review E* 1996; **55**:R21–R24.
15. Dubiner M. Spectral method on triangles and other domains. *Journal of Scientific Computation* 1991; **6**:345.
16. Sherwin SJ, Karniadakis GE. A triangular spectral element method; application to the incompressible Navier–Stokes equations. *Computers and Methods in Applied Mechanical Engineering* 1995; **123**:189–229.

Copyright © 2003 John Wiley & Sons, Ltd.

17. Coutanceau M, Bouard R. Experimental determination of the main features of the viscous flow in the wake of a circular cylinder in uniform translation. Part 1. Steady flow. *Journal of Fluid Mechanics* 1977; **79**(2):231–256.
18. Nieuwstadt F, Keller HB. Viscous flow past circular cylinders. *Computers and Fluids* 1973; **1**:59–71.
19. Clift R, Grace JR, Weber ME. *Bubbles*, *Drops*, *and Particles*. Academic Press: New York, 1978.
20. Goldstein S. *Modern Development in Fluid Dynamics*. Clarendon Press: Oxford, 1938.
21. Braza M, Chassaing P, Ha Minh H. Pressure velocity fields in the wake of a circular cylinder. *Journal of Fluid Mechanics* 1986; **165**:79–130.

Copyright © 2003 John Wiley & Sons, Ltd.